

# Geochemistry, Geophysics, Geosystems

## RESEARCH ARTICLE

10.1029/2020GC009512

Erica M. Nathan and Anant Hariharan contributed equally.

### Key Points:

- A total of 299 new teleseismic shear-wave splitting measurements have been made using broadband stations across Greenland
- Variations in splitting fast direction with back-azimuth can be explained by two layers of mantle anisotropy which are consistent across Greenland
- The lower layer of anisotropy is consistent with asthenospheric shear or accreted lithosphere; the upper layer is consistent with past lithospheric orogenic deformation

### Supporting Information:

Supporting Information may be found in the online version of this article.

### Correspondence to:

E. M. Nathan,  
erica\_nathan@brown.edu

### Citation:

Nathan, E. M., Hariharan, A., Florez, D., & Fischer, K. M. (2021). Multi-layer seismic anisotropy beneath Greenland. *Geochemistry, Geophysics, Geosystems*, 22, e2020GC009512. <https://doi.org/10.1029/2020GC009512>

Received 5 NOV 2020

Accepted 31 MAR 2021

## Multi-Layer Seismic Anisotropy Beneath Greenland

Erica M. Nathan<sup>1</sup> , Anant Hariharan<sup>1</sup> , Darien Florez<sup>1</sup> , and Karen M. Fischer<sup>1</sup> 

<sup>1</sup>Department of Earth, Environmental, and Planetary Sciences, Brown University, Providence, RI, USA

**Abstract** Seismic anisotropy provides insight into past episodes of lithospheric deformation and the orientations of strain in the underlying asthenosphere. The Greenland mantle has played host to a rich history of tectonic processes, including multiple orogenies and plume-lithosphere interactions. This study presents new measurements of SKS splitting that reveal strong variations in fast polarization direction with back-azimuth that are consistent across Greenland, including at stations where splitting measurements have not previously been reported. We compared observed fast polarization directions to the predictions of two-layer models with olivine-orthopyroxene anisotropy. The family of models that provides acceptable misfits at 95% confidence indicates an upper layer olivine a-axis azimuth of 222–236°, a lower layer olivine a-axis azimuth of 114–130°, and non-zero a-axis plunges. These models are consistent with an upper layer of lithospheric anisotropy due to Proterozoic and Archean orogenic fabrics, and a lower layer of anisotropy corresponding to either asthenospheric flow aligned approximately parallel to the direction of absolute plate motion and plunging due to lithospheric topography or dipping lithospheric structures created by episodes of paleo-convergence.

**Plain Language Summary** Measurements of seismic anisotropy (the direction-dependent variation in seismic wavespeed) provide useful information about the orientation of deformation in the Earth. We measured seismic anisotropy using shear waves refracted through the outer core and recorded by stations in Greenland. Due to new stations and data, this study includes more measurements of the effects of anisotropy than previously possible. We show that a model with two layers of anisotropy explains dominant patterns in the fast vibration direction of the shear waves as a function of the angle at which they approach each station. We suggest that the shallow layer reflects coherent deformation in the continental lithosphere of Greenland due to its history of plate collisions and that the lower layer reflects deformation in the asthenospheric mantle induced by the motion of the plate above or a second layer of lithospheric anisotropy.

## 1. Introduction

Nearly all of Greenland's bedrock geology is inaccessible because it is covered by the Greenland Ice Sheet. Therefore, geophysical investigations are especially important in furthering our understanding of Greenland's subglacial lithospheric structure. Greenland is a region of interest as its lithosphere contains cratonic material and records the history of Archean, Proterozoic, and Paleozoic orogenies and could provide insight into the history of the Iceland plume (e.g., Henriksen et al., 2009).

The majority of Greenland is Precambrian and has been modified by multiple tectonic (orogenic and rifting) events (e.g., Henriksen et al., 2009). Of particular note is the Trans-Hudson Orogeny, which was a widespread set of plate collisions that helped to build Laurentia around 1.8 Ga (e.g., St-Onge et al., 2009). Orogenic belts from this event can be found across North America; in Greenland, this includes the Rinkian and Nagssugtoqidian belts that bound major crustal blocks (e.g., Antonijevic & Lees, 2018; Dahl-Jensen et al., 2003; Henriksen et al., 2009). During the Silurian, the continent-continent collision of Laurentia and Baltica developed the Eastern Greenland Caledonides, resulting in complex thrust architecture along the eastern coast (e.g., Dawes, 2009; Higgins & Leslie, 2000). More recently, Greenland has been modified volcanically and thermally by the passage of the Iceland plume underneath Greenland between 70 and 40 Ma (e.g., Lawver & Müller, 1994). However, studies differ regarding the exact path of the plume under Greenland and its effects on the overlying lithosphere (Braun et al., 2007; Forsyth et al., 1986; Lawver & Müller, 1994; Steffen et al., 2018; Steinberger et al., 2019).

Regional-scale seismic imaging has helped elucidate this tectonic history, constrain the temperature and composition of the Greenland mantle, and interrogate plume-lithosphere interactions. Surface-wave tomography (Darbyshire et al., 2018; Lebedev et al., 2018; Levshin et al., 2001; Mordret, 2018) has detected thick, presumably depleted cratonic mantle lithosphere and lithospheric structures modified by multiple tectonic events. H-K stacking and synthetic modeling of receiver functions have helped to constrain regional crustal thickness and composition (Dahl-Jensen et al., 2003; Kumar et al., 2005; Kumar et al., 2007). Images from body-wave tomography (Toyokuni et al., 2020) show a NW-SE low-velocity anomaly within the mantle coincident with heat flow anomalies interpreted as evidence for plate movement over the Iceland plume. Surface-wave tomography (Lebedev et al., 2018; Levshin et al., 2017; Mordret, 2018; Pourpoint et al., 2018) has also been used to identify this thermal signature.

Seismic anisotropy is another metric that can be used to observe mantle deformation, and shear-wave splitting arises when anisotropic media polarize shear wave particle motions that travel at different velocities. The polarization direction of the fast shear wave ( $\phi$ ) and the time delay ( $\delta t$ ) between the two split waves measured at the receiver are commonly used to characterize the anisotropy. In the mantle, a common source of anisotropy is the lattice preferred orientation of minerals such as olivine and orthopyroxene. In conditions where the mantle is relatively low stress, horizontal flow results in mantle fabrics formed by the A, C, or E types of olivine lattice preferred orientation, producing shear-wave splitting fast polarization directions that are approximately parallel to the direction of horizontal flow; for dry mantle (A fabrics), olivine a-axes are also aligned close to the horizontal flow direction (Karato et al., 2008; Long & Becker, 2010). Shape preferred orientation of velocity heterogeneity can also cause anisotropy (Holtzman et al., 2003).

Large-scale mantle deformation processes that produce seismic anisotropy include asthenospheric flow and tectonic deformation in the lithosphere. In the simplest case of asthenospheric flow, shearing produced by the motion of the overlying plate aligns olivine a-axes and shear-wave splitting fast directions parallel to absolute plate motion (Silver & Chan, 1991; Vinnik et al., 1989). However, deflections of asthenospheric flow due to topography on the base of the lithosphere (e.g., Fouch et al., 2000; Miller & Becker, 2012) or broader mantle flow patterns (e.g., Long & Becker, 2010) may produce lateral variations in splitting fast directions relative to absolute plate motion. Deformation of the mantle lithosphere may involve strain that is coherent with crustal tectonic indicators of the most recent and/or significant deformation episode; for example, olivine a-axes and shear-wave splitting fast directions that are aligned parallel to the strike of orogenic belts, related thrust faults, and transpressional shear zones (e.g., Silver, 1996).

Relatively few studies of seismic anisotropy exist for the mantle beneath Greenland. Azimuthal anisotropy in global-scale images (Ekström, 2011; Schaeffer et al., 2016) is difficult to interpret due to the coarse sampling of these models, which provide only a small number of data points in Greenland. A regional-scale surface-wave study (Darbyshire et al., 2018) shows weak anisotropy at shallow mantle depths with a NW-SE fast direction beneath the central latitudes of Greenland and NE-SW fast directions in the far north and south, but only provides constraints in the uppermost mantle (depths of ~120 km and above). Previous shear-wave splitting measurements are predominantly N-NE in southern Greenland, and more variable elsewhere (e.g., Ucik et al., 2008). A lateral gradient in anisotropy near the southern coast of Greenland has also been measured with quasi-love waves (Servali et al., 2020).

The presence of multiple layers of anisotropy, with different olivine a-axis azimuth, a-axis plunge, and/or strength result in back-azimuthal variation of splitting parameters. This phenomenon is well understood, having been modeled using both analytical expressions for anisotropy in two layers (Savage & Silver, 1993) and simulations of waveform propagation through anisotropic media (e.g., Abt et al., 2010). Thus, when detected, back-azimuthal variations of apparent splitting parameters are a useful tool for measuring the variation of anisotropy with depth (e.g., Levin et al., 1999; Savage & Silver, 1993). In the most general case of multi-layer anisotropy, allowing for layers with plunging olivine a-axes, the measured splitting parameters will exhibit a  $2\pi$  periodicity in back-azimuth (e.g., Savage & Silver, 1993). However, if both layers in a two-layer setting are flat, measured splitting parameters exhibit a  $\frac{\pi}{2}$  periodicity with back-azimuth (Silver & Savage, 1994). With increasing relative strength of anisotropy in one of multiple layers, the measured parameters will converge to the case of a single layer of anisotropy, exhibiting little variation of splitting parameters with back-azimuth (Savage & Silver, 1993).

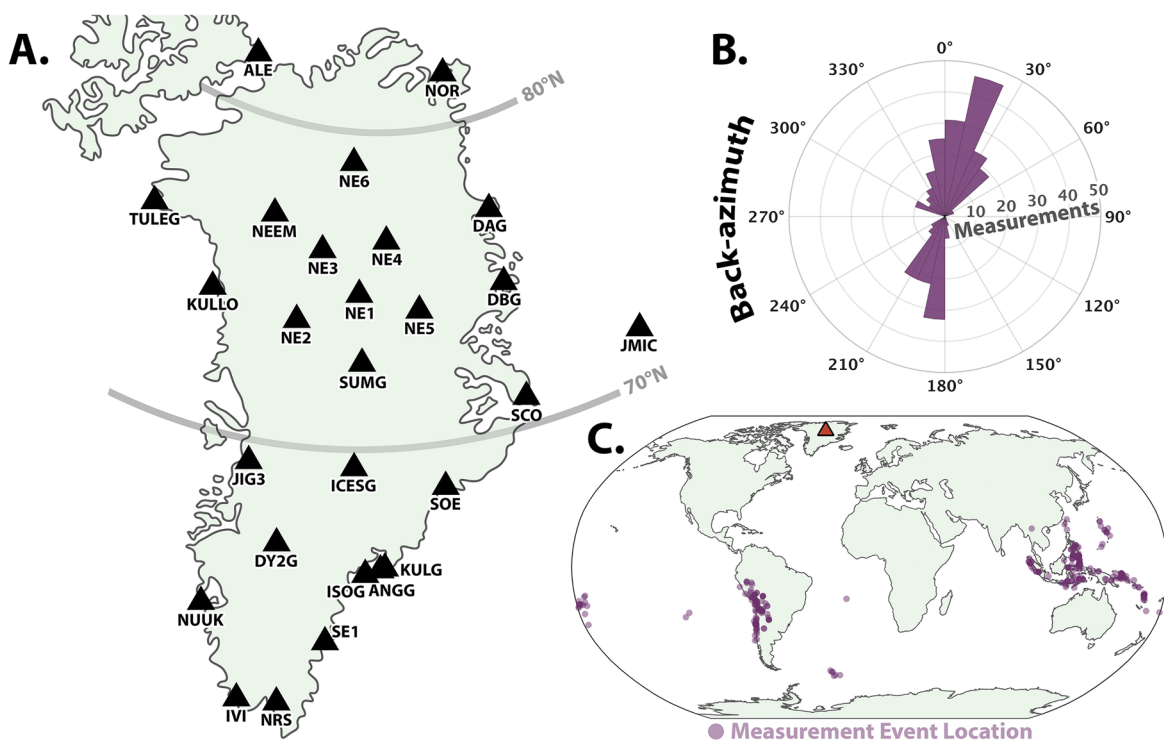


**Figure 1.** (a) Map of station locations used in this study (Table S1). (b) Polar histogram of the distribution of back-azimuths represented in measurements from this study. (c) Distribution of earthquake event locations for measurements included in our dataset (Table S2).

A range of approaches have been applied to constrain the location and orientation of anisotropy in depth, including exploration of the large model space using the neighborhood algorithm (e.g., Wookey, 2012; Yuan & Levin, 2014). Grid searches through model parameter space have also been used to constrain a-axis azimuth, plunge, and anisotropy strength (Abt et al., 2010). Forward modeling that parameterizes the anisotropy in each layer with a fast polarization direction and splitting time is also sometimes employed, reducing the parameter space (e.g., Aragon et al., 2017; Wookey, 2012). In a limited number of cases, tomographic approaches have been applied to shear-wave splitting from local (Abt & Fischer, 2008; Abt et al., 2009; Caixto et al., 2014) and teleseismic events (Long et al., 2008; Mondal & Long, 2020).

Although prior studies have measured shear-wave splitting in Greenland (Clement et al., 1994; Helffrich et al., 1994; Ucik et al., 2008; Ucik et al., 2005; Vinnik et al., 1992), clear variations in splitting parameters with back-azimuth diagnostic of multiple layers of anisotropy have not been resolved (e.g., Ucik et al., 2008). In this study, we measure shear-wave splitting across Greenland using decades of new data and 16 new stations, observe systematic variations in fast polarization direction with back-azimuth, and model these patterns with two layers of anisotropy. The resulting constraints on anisotropy parameters in the two model layers shed new light on the relationships between mantle deformation fabrics, past episodes of lithospheric deformation, and the nature of recent mantle flow beneath Greenland.

## 2. Data and Methods

### 2.1. Data

We measured shear-wave splitting fast polarizations and delay times from  $^{\ast}$ KS phases (SKS, SKKS, PKS, sSKS, pSKS, and combinations thereof) using a new dataset collected from 27 stations (Figure 1a) deployed on the Greenland ice sheet and coast, as well as stations on Ellesmere Island (ALE) and on Jan Mayen Island (JMIC) (Table S1). Seismic data used in this analysis were acquired at broadband stations, which were deployed for different periods of time (Table S1) ranging from 4 months (for stations part of temporary deployments) to nearly 30 years. Stations include those from network codes DK (the Danish Seismological

# Splitting Measurement

Event: 08-Jul-2008 (190) 09:13 -15.99N -71.75E 123km Mw=6.2  
 Station: SUMG Backazimuth: 211.9° Distance: 91.08° SNRsc: 16.0

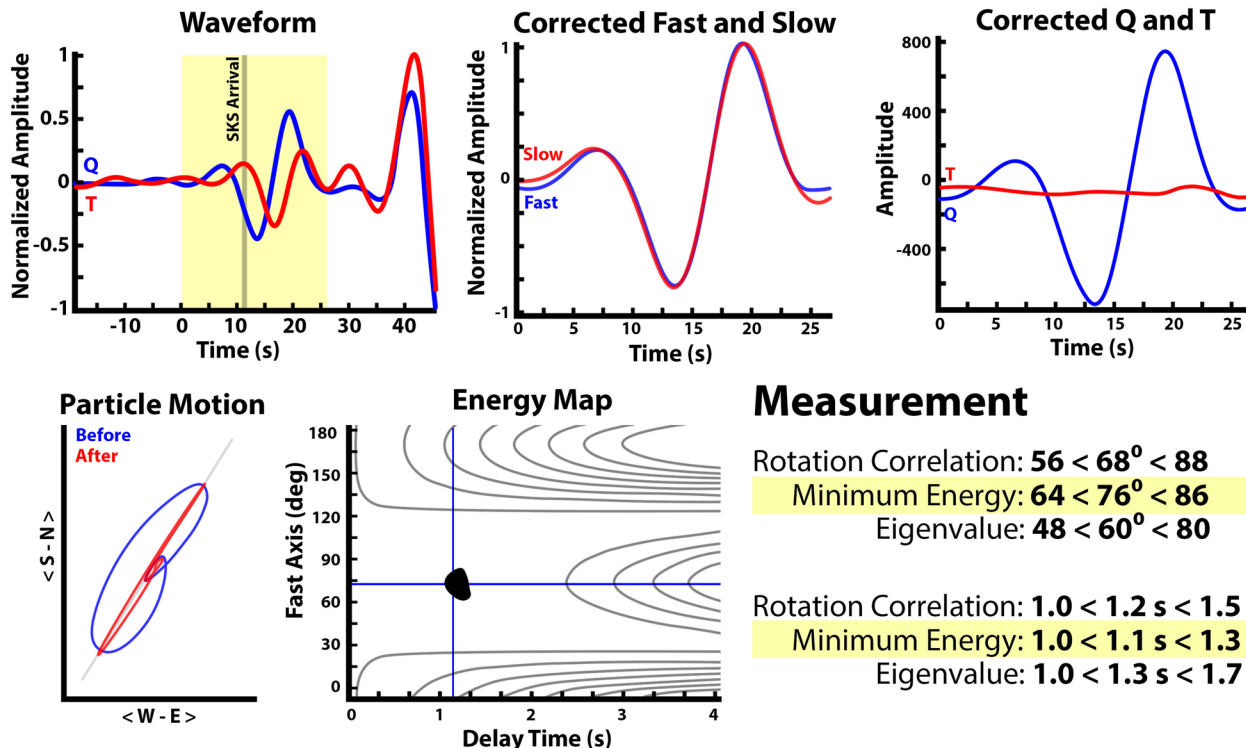


**Figure 2.** Example of a high-quality splitting measurement obtained using SplitLab (Wüstefeld et al., 2008). Upper left: Q and T components of initial waveforms. An SKS phase is highlighted in the yellow window, with the gray line showing the IASP91-predicted arrival time. Upper center: SKS phase waveform on fast and slow polarization components, shifted to remove the splitting lag time. Upper right: the shifted waveform components on the Q and T components. Lower left: horizontal components of the SKS phase before (blue) and after (red) the splitting lag time was removed. Lower center: surface of energy on the T component as a function of trial splitting fast direction and delay time. Splitting parameters within 95% confidence of the best-fitting values lie within the shaded contour. Lower right: fast direction and splitting time (with uncertainties) for each of the measurement methods.

Network), GE (GEOFON), XF (GLISN), G (GEOSCOPE), CN (Canadian National Seismograph Network), and II (the IRIS/USGS Global Seismographic Network) (Table S1). Station spacing varies dramatically, from more than 200 km on the ice sheet to less than 50 km on the coast, with stations mostly distributed along the coast. We employed BH\* channels, resampled at 20 Hz in SplitLab (Wüstefeld et al., 2008). We selected earthquakes of magnitude greater than 6.0, between epicentral distances of 90° and 130° from each station (Figures 1b and 1c).

## 2.2. Measurement Methods

To measure shear-wave splitting, we employed the SplitLab software (Wüstefeld et al., 2008). We rotated waveforms from an ENZ to an LQT coordinate system; the L component is in the ray plane and points along the raypath from the source to the station, the Q component also points in the direction to the source, in the same plane but is orthogonal to the L component, and the T component is orthogonal to both. We filtered waveforms between 0.01 and 0.1 Hz before manually inspecting and windowing data around the \*KS phase. We report results of the transverse-component minimization method (Silver & Chan, 1991), although we only retained measurements whose uncertainties overlapped those from the eigenvalue minimization method. We imposed several other criteria to distinguish a measurement as high quality (e.g., Figure 2): the \*KS phase is a clear arrival with a signal-to-noise ratio  $\geq 2$  on the Q component; \*KS phases (isolated or coincident) behave like a split \*KS phase, that is, the energy on the transverse component decreases

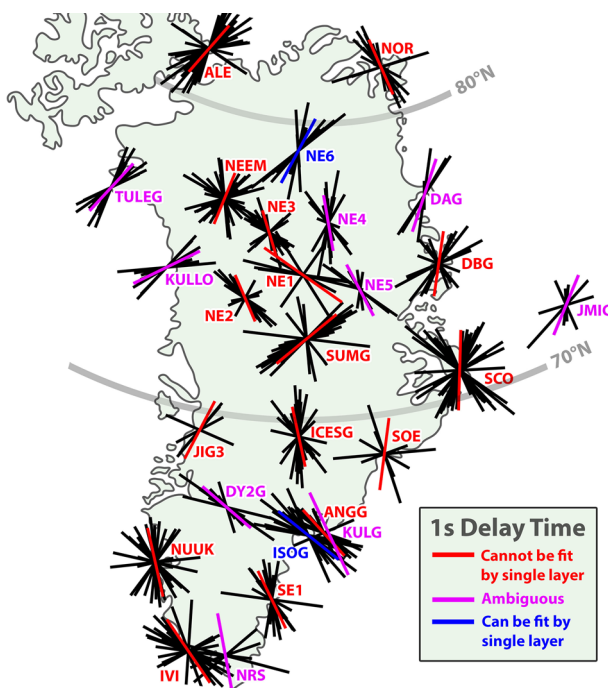


**Figure 3.** Map of individual splitting measurements (black lines) and average fast direction (colored lines) measured at each station. Color shows classification of whether the fast directions at the station can or cannot be fit by a single layer of anisotropy. The length of the lines corresponds to splitting time; the time scale appears in the legend.

produce the minimum summed circular misfit when compared to the observed fast directions at the station. Our measurements fall into three back-azimuth ranges of width 120°. If the maximum misfit (with respect to the best-fitting a-axis orientation) to a single observation in any cluster is greater than 30°, we deem the fast directions as not fit by a single layer. Stations are deemed ambiguous if the maximum circular misfit is less than 30° for all observed fast directions, but data do not exist in all three back-azimuth bins, which could result in under-sampling of the predictions of an underlying two-layer anisotropy pattern. Using this definition, only stations NE6 and ISOG are consistent with a single layer of anisotropy (Figure 3).

In addition, when all fast polarizations are plotted together (Figure 4b), their overall pattern of fast direction variation with back-azimuth is broadly consistent, including stations which can and cannot be fit by a

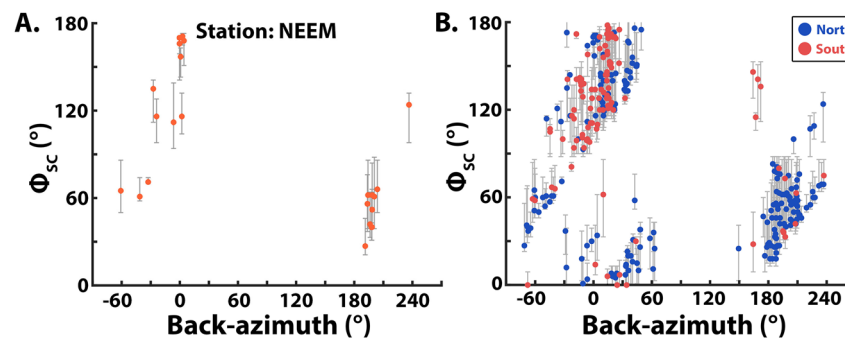


**Figure 4.** (a) Fast directions versus back-azimuth at station NEEM. Significant variation in fast direction occurs which cannot be explained by a single layer of anisotropy. Plots for all other stations can be found in Figures S1a and S1b. (b) All measurements of fast direction as a function of back-azimuth for our study area separated into northern ( $<70^{\circ}\text{N}$ ) and southern ( $<70^{\circ}\text{N}$ ) groups based on station latitude.  $N = 299$ .

and elliptical particle motion becomes linear when splitting is removed from the waveforms; the 95% error surfaces for the transverse-component minimization method and eigenvalue minimization method are close to an ellipse; the uncertainty range in splitting time does not overlap zero nor does it exceed 4 s; the uncertainty in fast direction is less than  $\pm 30^{\circ}$  for the transverse-component minimization method. Note that the formulation for uncertainty used here is from Silver and Chan (1991) and is thus slightly different from the modified version put forth by Walsh et al. (2013).

### 3. Results

#### 3.1. Shear-Wave Splitting Results

We measured a total of 299 high-quality shear-wave splitting measurements (Table S2). At many stations, there is a significant variation in the measured fast directions with back-azimuth (Figure 3 and Figures S1a and S1b). In particular, the stations with the largest number of measurements (e.g., ALE, NEEM, SCO) all show clear variation in fast direction with back-azimuth. For example, at station NEEM (Figure 3a), fast directions span 27–171°. At other stations, the fast directions are clustered around a single value (e.g., NE6, TULEG, KULLO, DAG, ISOG). However, at some stations, the distribution of measurements with back-azimuth is insufficient to determine whether back-azimuthal variation in fast direction exists. In addition, there is little geographic coherence in mean fast direction between stations (Figure 3 and Figure S1).

To examine whether measurements at individual stations can be fit by a single layer of anisotropy, we determined the single horizontal olivine a-axis orientation whose predicted shear-wave splitting fast directions

single layer of anisotropy (Figure 3 and Figures S1a and S1b). This broad pattern of fast direction variation in back-azimuth (Figure 4b) persists in regional sub-groups of stations, for example, those north and south of 70°N (Figure 4b).

### 3.2. Modeling Two Layers of Anisotropy

To constrain the variation of anisotropy with depth implied by the observed variation of shear-wave splitting fast directions with back-azimuth, we compared observed fast directions to the predictions of two-layer anisotropy models. We assumed an isotropic crust of thickness 40 km (Darbyshire et al., 2018), an anisotropic mantle lithosphere between 40 and 150 km, and an anisotropic asthenosphere between 150 and 300 km. The mantle lithosphere thickness is based on thermally defined lithospheric thickness values for Greenland (Steinberger & Becker, 2018). However, the vertical thicknesses of these anisotropic layers is unconstrained as the layer thicknesses and the strength of anisotropy in each layer can trade off with each other, both of which impact the back-azimuthal variation of splitting parameters in a similar manner. To define the tensor of anisotropic elastic coefficients, we assumed a mantle composed of 70% olivine and 30% orthopyroxene. The model has six free parameters: olivine a-axis azimuth ( $\theta$ ) and plunge ( $\delta$ ), and anisotropy strength ( $\alpha$ ) in each of the two layers. Anisotropy strength is defined as the percentage of total single-crystal anisotropy. In other words, 100% anisotropy would be the elastic coefficients for pure olivine and orthopyroxene, aligned with respect to each other so that the a-axis of olivine is parallel to the c-axis of orthopyroxene and the b-axis of olivine is parallel to the a-axis of orthopyroxene (Mainprice & Silver, 1993). For a horizontal olivine a-axis, the c-axis is horizontal and the b-axis is vertical. The (orthorhombic) single-crystal elastic tensor of olivine is taken from Anderson and Isaak (1995) and Abramson et al. (1997) with pressure and temperature derivatives from Abramson et al. (1997) and Anderson and Isaak (1995), respectively. The orthopyroxene elastic tensor and derivatives are from Frisillo and Barsch (1972).

We predicted shear-wave splitting parameters for each back-azimuth in the observed splitting dataset using the approximate particle motion perturbational method (Fischer et al., 2000); this approach has been shown to match results generated using pseudospectral synthetics (Hung & Forsyth, 1998). The code rotates and time-shifts an initial linear wavelet of period 10 s using the Christoffel matrix for the anisotropy in the lower layer and then rotates and time-shifts the resulting particle motion for the anisotropy in the upper layer. We assumed an incidence angle suitable for \*KS waves of 10°, treating all phases the same way in the modeling. Shear-wave splitting parameters were measured from the synthetic waveform using the eigenvalue minimization method (Silver & Chan, 1991), which for the noise-free synthetics used in the modeling yields identical results to the transverse energy minimization method that was applied to the data.

Because of the non-linear relationship of anisotropy model parameters to shear-wave splitting predictions, we employed a grid-search approach to determine the best-fitting model parameters. Due to the large number of model parameter combinations, we first compared the observed fast directions to predicted fast directions from a more coarsely sampled grid of parameters, and then implemented a finer grid search around the minima resolved from the coarser grid. In the coarse grid search, a-axis azimuth varies in increments of 10° between 0° and 360° from north, a-axis plunge varies in increments of 10° between 0° and 50° from horizontal, and the strength of anisotropy varies in increments of 10% between 0% and 50%. In the finer grid search, we probed a-axis azimuths in increments of 2° in a range  $\pm 20^\circ$  away from the best-fitting value from the coarse grid search with plunge and strength parameters at the same spacing as in the coarse grid search; we also allowed plunge values in the deeper layer to vary to 70° instead of 50° to ensure our best-fitting result did not lie on the edge of the parameter space explored in the grid search, and thus also probed dips of 60° and 70° in the lower layer.

Using the measurements of fast directions from all stations (Figure 4b and Table S2), the coarse grid search produced a global minimum RMS misfit of 2.81 at  $\theta_{\text{deep}} = 130^\circ$ ,  $\delta_{\text{deep}} = 40^\circ$ ,  $\alpha_{\text{deep}} = 50\%$ ;  $\theta_{\text{shallow}} = 230^\circ$ ,  $\delta_{\text{shallow}} = 30^\circ$ ,  $\alpha_{\text{shallow}} = 40\%$  (Figure 5). There are other local minima, but these do not minimize misfit. The finer grid search produced a better-fitting model with a misfit of approximately 2.26 (Figure 4). The best-fitting parameters for the finer grid search are  $\theta_{\text{deep}} = 124^\circ$ ,  $\delta_{\text{deep}} = 50^\circ$ ,  $\alpha_{\text{deep}} = 50\%$ ;  $\theta_{\text{shallow}} = 226^\circ$ ,  $\delta_{\text{shallow}} = 20^\circ$ ,  $\alpha_{\text{shallow}} = 40\%$ . We used an F-test (Snedecor & Cochran, 1991) to determine the family of models that fit the observations within the 95% confidence limits of the best-fitting model.

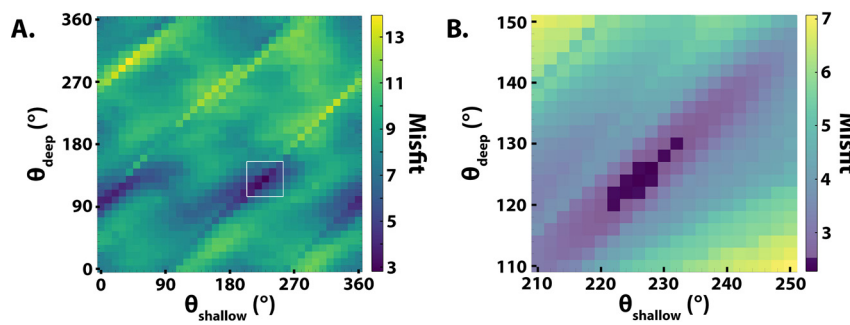


**Figure 5.** (a) Misfit surface along a constant  $\delta_{\text{deep}} = 40^\circ$ ,  $\alpha_{\text{deep}} = 50\%$ ,  $\delta_{\text{shallow}} = 30^\circ$ , and  $\alpha_{\text{shallow}} = 40\%$  showing variation in misfit as a function of  $\theta_{\text{deep}}$  and  $\theta_{\text{shallow}}$ . The best-fitting model from the coarse grid search is at  $\theta_{\text{deep}} = 130^\circ$ ,  $\delta_{\text{deep}} = 40^\circ$ , and  $\alpha_{\text{deep}} = 50\%$ ;  $\theta_{\text{shallow}} = 230^\circ$ ,  $\delta_{\text{shallow}} = 30^\circ$ , and  $\alpha_{\text{shallow}} = 40\%$  with a misfit of 2.8145. This model does not satisfy the *F*-test criterion corresponding to the finer grid search. The a-axis range probed in the finer grid search, which encloses the best-fitting model from the coarse grid search, is outlined in white. (b) As in left, but for the finer grid search. This misfit surface is along constant  $\delta_{\text{deep}} = 50^\circ$ ,  $\alpha_{\text{deep}} = 50\%$ ,  $\delta_{\text{shallow}} = 20^\circ$ , and  $\alpha_{\text{shallow}} = 40\%$ . The darkened region in the right panel indicates parameters that lie within the 95% confidence *F*-test limits of the best-fitting model.

From the fine grid search, we found a total of 95 models that satisfy the 95% confidence interval constraint and adequately predict the large-scale variation of splitting fast direction with back-azimuth (Figure 6, left). As the width of the parameter histograms (Figure 6, right) indicate, our grid search places robust constraints on the a-axis azimuths in the upper and lower layers. Acceptable a-axis azimuths in the upper layer vary from  $222^\circ$  to  $236^\circ$  and in the lower layer from  $114^\circ$  to  $130^\circ$ . Acceptable values of a-axis plunge in the lower layer vary from  $50^\circ$  to  $60^\circ$ , while acceptable values of a-axis plunge in the upper layer range from  $10^\circ$  to  $30^\circ$ . Among the parameters in our grid search, the strength of anisotropy in each layer is the least well constrained. Unlike a-axis azimuth or plunge, it does not result in sharp discontinuities in the variation of splitting fast direction with back-azimuth, and the model misfits are thus the least sensitive to it. Furthermore, the strength of anisotropy trades off with the thickness of each layer, as well as with the a-axis plunge (Abt et al., 2010). Nonetheless, the large values of strength highlight distinct and strong anisotropy in each layer.

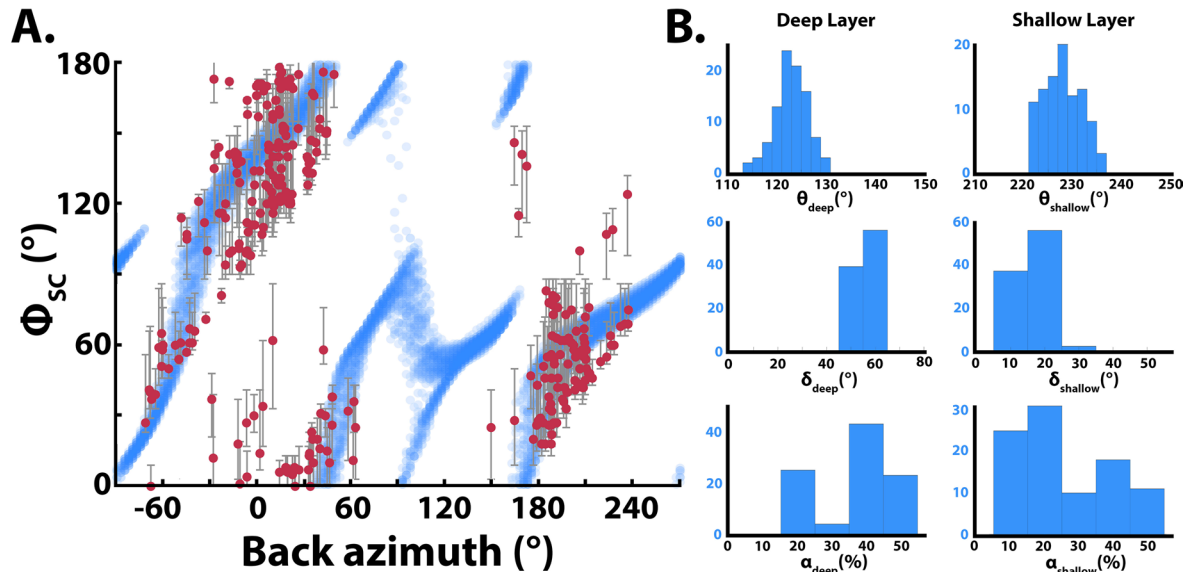


**Figure 6.** (a) Suite of best-fitting model predictions of splitting fast direction (blue) as a function of back-azimuth, obtained from the fine grid searches that satisfy the misfit criterion corresponding to the *F*-test at 95% confidence level, overlain on the splitting fast direction measurements from this study (red). (b) Histograms of the model parameters satisfying the misfit criterion.

The delay times we measure exhibit significant scatter (Figures S1c, S1d, and S2). Due to this, back-azimuthal variation in the delay times is not discernable and the distribution of delay times is fairly unimodal, centered on a mean of  $\approx 1.7$  s, albeit with a large standard deviation of  $\approx 0.5$  s. As a result, we follow the convention used in some mantle-scale shear-wave splitting studies (Aragon et al., 2017; Dubé et al., 2020) and do not attempt to incorporate predictions of variations in delay times in our modeling for the best-fitting model parameters in each layer.

To investigate how the non-uniform back-azimuthal sampling of fast direction patterns affects the resolvability of model parameters, we conducted a series of tests on synthetic datasets that have the same back-azimuthal distribution as the observed fast directions. One test explores the case in which two-layer anisotropy has the same mean model parameters as the model that best fits the data, but the parameters are allowed to vary about those means following a Gaussian distribution with a standard deviation of  $30^\circ$  for a-axis azimuth,  $10^\circ$  for a-axis plunge, and 10% for anisotropy strength. This case is intended to represent deformation as a function of depth which is similar across Greenland but varies laterally to a moderate degree. From this distribution of model parameters, a set of model parameters was drawn and fast directions were predicted for each back-azimuth in the real dataset for 50 different draws of model parameters. To generate the synthetic dataset, we drew a value at every back-azimuth from one of the 50 different splitting fast direction predictions. The model which best fits the synthetic dataset was then determined using the coarse grid of model parameter predictions. One iteration is shown in Figure 7a. This process was repeated 100 times, and the resulting distribution of best-fitting model parameters is shown in Figures 7c–7h (blue histograms) together with the input distribution of model parameters (pink histograms). The retrieved model parameters are broadly similar to the input distribution of model parameters, in particular for the upper and lower layer a-axis azimuths which are the best resolved model parameters. This result supports the argument that meaningful anisotropy parameters can be retrieved from fast direction data, even when the underlying model varies moderately.

In a second test, the possibility that sub-regions have simpler single-layer anisotropy was added to the first scenario. In this test, 50% of the 50 model parameter sets come from the Gaussian distributions about the best-fitting two-layer model (as in Figure 7a) and 50% are drawn from a distribution of one-layer anisotropy models. (We note that one-layer models are consistent with cases where the a-axis orientation in an upper and lower layer are similar.) In the one-layer model distribution, horizontal a-axis azimuths have means of  $50^\circ$  and  $115^\circ$ , each with a standard deviation of  $15^\circ$ . Again, the process is repeated 100 times, and the resulting best-fitting model parameters are shown in Figures 7i–7n. Although the introduction of the one-layer models produces larger differences between the retrieved (blue) and input (pink) two-layer model parameter distributions, the retrieved a-axis azimuths fall within the input distribution. This result indicates that retrieved two-layer a-axis azimuths can be obtained not only when the underlying model varies moderately but also when the regional dataset reflects sub-regions that contain one-layer anisotropy.

Additional synthetic tests are described in the supplement (Figures S7–S9 and Text S1). These tests include a scenario in which the fast directions at each back-azimuth are randomly drawn from the total distribution of fast directions (Figure S9). This test is equivalent to assuming that each synthetic fast direction represents a localized region of one-layer anisotropy and that any apparent pattern of fast direction with back-azimuth is coincidental. For 100 versions of this case, the resulting distribution of retrieved two-layer models contain model parameters across the range of possible values, and a-axis azimuth ranges for each layer are not well constrained. These results fundamentally differ from those produced by fitting the observed fast directions. We conclude that the observed pattern of fast direction versus back-azimuth in Greenland is not coincidental, and that two-layer anisotropy (or at least depth-varying anisotropy) is required.

## 4. Discussion

### 4.1. Comparison to Prior Studies of Anisotropy

Previous work in Greenland has suggested that significant differences in crustal azimuthal anisotropy exist between northern and southern Greenland (Darbyshire et al., 2018). However, we do not find any significant difference in the back-azimuthal pattern of fast directions between these regions (Figure 4b). We separately modeled the splitting observations for the northern and southern groups of stations; the resulting ranges of

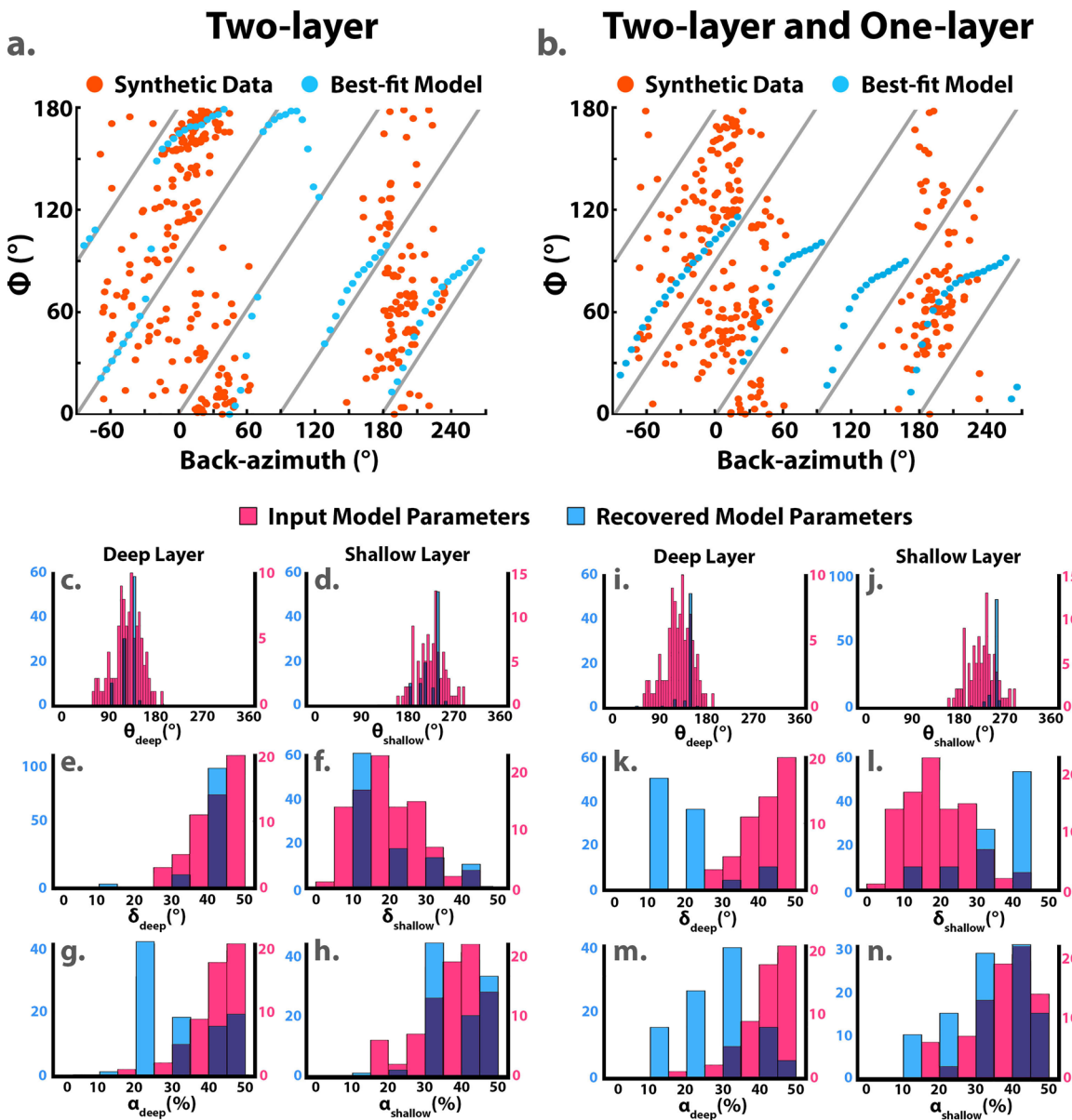


**Figure 7.** Synthetic test that explores how moderate random variation in two-layer model parameters impacts recovery of their distribution, without (a, c–h) and with (b, i–n) additional one-layer anisotropy. (a) One example of synthetic data (orange points) that are predictions of an input model where parameters are drawn from a Gaussian distribution where the mean is from the best-fitting model for the observed Greenland fast directions. Predictions of the retrieved model (blue) that best fits the synthetic data. Gray lines are null lines. (c–h) Distributions of model parameters recovered from fitting synthetic data (blue bars) for 100 cases of model parameters (pink bars) drawn from a Gaussian distribution where the mean is from the best-fitting model for the observations. (b) One example of synthetic data (orange points) that are predictions of a set of input models where 50% are drawn from a Gaussian distribution as described in (a) and 50% are drawn from one-layer models. (i–n) Distributions of model parameters recovered from fitting synthetic data (blue bars) for 100 cases of model parameters (pink bars) as described in (b).

two-layer model parameters for the two regions overlap, and the peaks of the a-axis azimuth distributions differ by no more than  $10^\circ$  (Figure S5). We also do not detect a difference in the pattern for stations on the Greenland ice sheet versus those on the coast (Figure S3). Although ice is an anisotropic mineral, the likely contribution from the ice sheet to total splitting observed should be small, especially because there is likely not a coherent fabric throughout an entire column of ice within the ice sheet (e.g., Bentley, 1972; Harland et al., 2013; Smith et al., 2017; Thorsteinsson, 2000; Thorsteinsson et al., 1997). Although we cannot rule out the presence of smaller-scale lateral variations in anisotropy parameters (for example, depth-varying

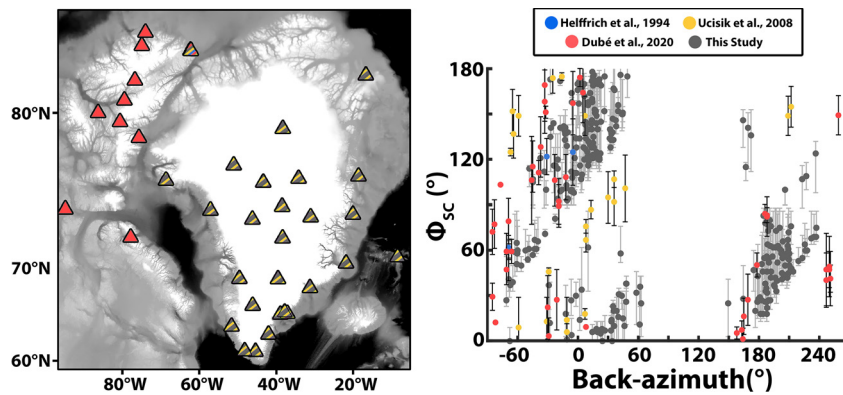


**Figure 8.** Left: locations of stations outside of and in Greenland used in certain other studies. Colors are the same in the map and back-azimuth plot. Right: comparison of our shear-wave splitting fast polarizations (gray) with the results from other studies.  $N_{\text{otherstudies}} = 70$ .

anisotropy is not required at all stations, e.g., Figure 3) the back-azimuthal variation in splitting fast direction and the range of best-fitting anisotropy model parameters are broadly consistent across Greenland.

The widespread coherence of back-azimuthal fast direction variation across the entirety of Greenland is a key feature of our results. Comparison of shear-wave splitting measurements from some previous studies in Greenland and the Canadian high arctic (Dubé et al., 2020; Helffrich et al., 1994) indicates broad agreement (Figure 8) with the back-azimuthal dependence of the fast direction observed here. However, the fast direction distribution with back-azimuth from Ucik et al. (2008) is less similar. Strong fast direction variations with back-azimuth were found in some studies from other regions of the Canadian shield (Figure S6), but differences in these patterns relative to those in this study suggest regional variations in anisotropic parameters (Bastow et al., 2011; Darbyshire et al., 2015; Liddell et al., 2017; Snyder et al., 2013).

Among published models of azimuthal anisotropy, the regional models based on group velocity from Darbyshire et al. (2018) provide information at lateral scales most comparable to our results. At shallow mantle depths, Darbyshire et al. (2018) indicate NE-SW fast directions in the far north and south of Greenland, which are consistent with a-axis azimuths in the lithospheric layer of the best-fitting models found here, and NW-SE fast direction beneath the central latitudes of Greenland, which do not agree with our lithospheric parameters. However, the Darbyshire et al. (2018) group velocity results indicate weak anisotropy at mantle depths and represent constraints on only the shallow lithospheric mantle, leaving open the possibility that the two studies are compatible.

#### 4.2. Interpretation of Two-Layer Anisotropy Models in Terms of Mantle Deformation

A simple, first-order prediction for shear in the asthenosphere is that it would be driven by absolute plate motion, resulting in olivine a-axis azimuths that are parallel to absolute plate motion. Olivine a-axes in the deeper layer of the two-layer anisotropy models that provide acceptable fits to the observed Greenland fast directions (114–130°) are approximately aligned with absolute plate motion in Greenland assuming the no-net-rotation reference frame plate motion model of Argus et al. (2011); fixed hotspot reference frame models predict plate motion directions (60–70°) that differ from the deep layer a-axis azimuth range, but hybrid moving hotspot models agree well with the measured deep layer a-axis azimuths (Gripp & Gordon, 1990; Seton et al., 2012).

Consistency of asthenospheric a-axis azimuths and plate motion shear differs from the conclusions of some previous studies of anisotropy (Darbyshire et al., 2015; Liddell et al., 2017). These studies assert that asthenospheric anisotropy parallel to plate motion should not be expected, because the North American plate speed (~20 mm/yr) is slower than what is required (~40 mm/yr) to develop basal drag fabric (Debayle & Ricard, 2013). However, the 40 mm/yr threshold (Debayle & Ricard, 2013) refers to whole-plate alignment of fabric with plate motion. Indeed, Debayle and Ricard (2013) state that, for slow moving continental plates, the correlation between asthenospheric fabric and plate motion is more complicated, but that agreement

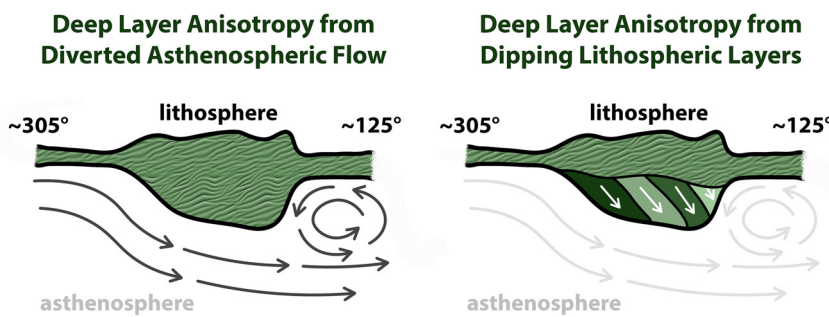


**Figure 9.** Left: schematic model for the end-member case where plunging a-axes in the lower layer of anisotropy are due to asthenospheric mantle flow around the base of thick cratonic lithosphere. The shape of the cratonic lithosphere in this profile is based on Mordret (2018) at latitudes of 70°N. Right: schematic model of the end-member case where plunging a-axes in the lower layer of anisotropy are lithospheric and due to dipping layers related to collisional accretion of the lithosphere.

can persist over large scales, citing central and eastern North America as an example. Thus, when considering a study region which is smaller than an entire plate, slow plate velocities do not rule out asthenospheric fabric in agreement with plate motion, either from basal drag or secondary convection (Debayle & Ricard, 2013).

We also compared the parameters of the deeper layer of anisotropy to models of mantle flow that account for mantle temperature, buoyancy, viscosity, and plate motion boundary conditions. However, due to different boundary conditions and other model assumptions, predictions for asthenospheric flow directions beneath Greenland differ between studies; it is possible to find models which are broadly consistent with the acceptable a-axes found here, such as some models in Conrad and Behn (2010) and Marquart et al. (2007), or inconsistent (e.g., Colli et al., 2018; Mihalffy et al., 2008).

The agreement between our well-constrained deep layer a-axis fast directions and the no-net-rotation plate motion directions from Argus et al. (2011) makes a strong case for asthenospheric anisotropy produced by shearing due to plate motion. However, the fact that acceptable a-axis plunges are  $\sim 50^\circ$  from horizontal pose a complication for this model. Even though a-axis plunge is less well-resolved than a-axis azimuth in the two-layer modeling, models with near-horizontal lower layer a-axes produce significantly worse fits to the observed fast polarization directions (Figure S4). We propose two models to explain the large and robust a-axis plunges in the lower layer of anisotropy, and note that they are not mutually exclusive.

In the first model, the deeper layer of anisotropy represents the asthenosphere and the large a-axis plunges are the result of asthenospheric flow diverted around basal lithospheric topography (Figure 9, left). In the regional shear-wave velocity model of Mordret (2018), high velocity zones consistent with thick cratonic mantle lithosphere lie beneath the central longitudes of Greenland, surrounded by lower velocities that are interpretable as thinner lithosphere and asthenosphere to the west and east. Assuming absolute plate motion at an azimuth of  $130^\circ$ , as would be predicted in the no-net-rotation reference frame of Argus et al. (2011), the asthenosphere would be shearing to the right relative to the lithosphere. Where the asthenosphere encounters thickening lithosphere, it would be diverted downward, producing a-axis plunges as found in the deeper layer of anisotropy in our models (e.g., Fouch et al., 2000). On the downwind side of the thick cratonic lithosphere, where lithospheric thickness decreases rapidly, edge-driven convection combined with plate motion shear can produce a local convection cell (e.g., Till et al., 2010). This circulating flow also has potential to produce a-axis plunges toward  $130^\circ$  in its lower left quadrant. In this scenario, not all regions of the asthenosphere have a uniform plunge, but plunges toward  $130^\circ$  are widespread enough that this is the plunge that best fits the entire Greenland shear-wave splitting dataset. Modest horizontal deflection of olivine a-axes around the lateral margins of the thick cratonic lithosphere would be predicted in this model (Fouch et al., 2000). However, because of the lateral extent of the thick Greenland lithosphere (Mordret, 2018), much of this deflection would lie outside of the region sampled by shear-wave splitting in this study.

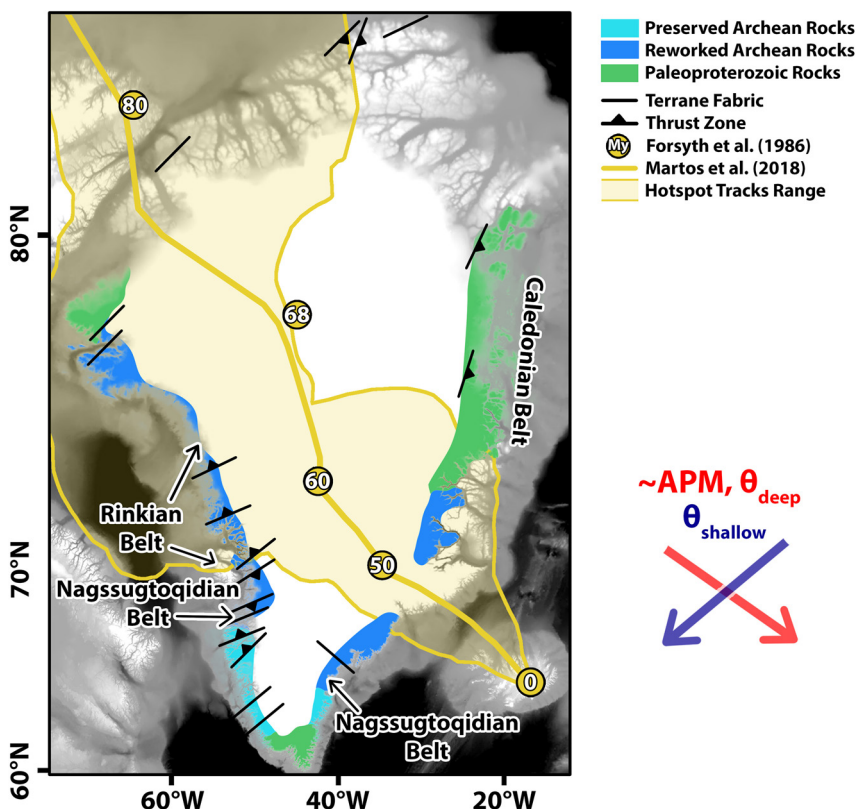


**Figure 10.** Map of relevant geology and tectonic features. Underlying gray field is ETOPO1 topography (Amante & Eakins, 2009) with basement ages, terrane fabrics, thrust zones, and orogenic belts from Henriksen et al. (2009), Dawes (2009), Higgins and Leslie (2000), Sanborn-Barrie et al. (2017), van Gool et al. (2002), and Von Gosen and Piepjohn (1999). The yellow-shaded region represents the extent of previously proposed hotspot tracks as compiled in Martos et al. (2018); the bold yellow line is their proposed hotspot track. Numbers show hotspot surface projections at different times from Forsyth et al. (1986). We also include the APM direction over central Greenland, as well as the best-fit a-axis orientations in the upper and lower layers.

In the second model, the lower layer of anisotropy is associated with dipping layers in the lithosphere as opposed to having an asthenospheric origin (Figure 9, right). This explanation has been used to interpret shear-wave splitting observations in both Fennoscandia (Grund & Ritter, 2020) and in the Hudson Bay region of Canada (Liddell et al., 2017). In northern Fennoscandia, Grund and Ritter (2020) resolved plunging anisotropy in a deeper layer. Building on a model proposed by Babuška et al. (1993), they explained this result with successive episodes of collision and subduction that created multiple zones of underthrust lithosphere in which initially horizontal olivine a-axes now plunge downward parallel to lithospheric dip. Similarly, Liddell et al. (2017) found back-azimuthal variations of splitting parameters that indicated plunging a-axes, and they interpreted this result in the context of underthrusting of the Superior plate as a result of collision. An independent observation consistent with the idea of imbricated lithosphere in Greenland comes from a dipping interface imaged by receiver functions along a dense transect in eastern Greenland; this structure was interpreted as a fossil subduction zone of eclogitized crust associated with eastward subduction prior to the main westward collision in this region during the Caledonian orogeny (Schiffer et al., 2014).

The relationship between the shallow layer a-axis azimuths inferred from the modeling ( $222\text{--}236^\circ$ ) and lithospheric deformation fabrics is difficult to evaluate because the Greenland ice sheet occludes much of the geologic evidence typically used to compare lithospheric anisotropy fabrics with the deformation signatures of major tectonic events (Von Gosen & Piepjohn, 1999). Nonetheless, inferred a-axis azimuths are consistent with deformation fabrics from Proterozoic and Archean orogenic events in western and northern Greenland (Figure 10). The Trans-Hudson Orogeny, which occurred 1.8 Ga, is responsible for Greenland's prominent Nagssugtoqidian belt, although the direction of compression and shape of the tectonic boundary

is obscured by the ice sheet and has been interpolated in many ways across Greenland (Antonijevic & Lees, 2018; Dawes, 2009; Henriksen et al., 2009; Pourpoint et al., 2018). Unobscured by the ice sheet, shear zones in Western Greenland closely associated with the Nagssugtoqidian orogen trend ENE-WSW to NE-SW (Bak et al., 1975; van Gool et al., 2002), parallel to local thrust zones and older Archean terranes (Henriksen et al., 2009; Korstgård et al., 1987; van Gool et al., 2002). NW-directed thrusting has also been inferred in the Proterozoic Rinkian orogen to the north in western Greenland (Sanborn-Barrie et al., 2017; van Gool et al., 2002) and in thrust zones at Greenland's northern margin (Von Gosen & Piepjohn, 1999). These indicators of lithospheric deformation are consistent with acceptable a-axis azimuths from the two-layer anisotropy modeling, and this agreement suggests that similarly oriented deformation fabrics are also present beneath the ice sheet (Figure 10).

However, deformation indicators in eastern Greenland are less consistent with the overall NE-SW acceptable lithospheric a-axis orientations (Figure 10). In southeastern Greenland, van Gool et al. (2002) infer an ESE structural grain. At two stations within this zone (ANGG and KULG), fast directions are predominantly NW-SE, raising the possibility that lithospheric deformation in this zone is rotated from the shallow layer trend indicated by the modeling of the complete set of Greenland stations. In addition, thrust fronts in the Paleozoic Greenland Caledonides are oriented ~N-S (Dawes, 2009). This inconsistency with the overall NE-SW-oriented shallow layer a-axis orientation may reflect an unresolved local variation in lithospheric a-axis alignment or that lithospheric fabric associated with the Caledonian orogeny was limited in its depth extent, possibly due to decoupling of the Laurentian retro-lithosphere (Hodges, 2016).

Local deformation associated with rifting has impacted both eastern and western Greenland at differing scales. The orientation of extension associated with Labrador sea rifting in the west is parallel to the shallow layer a-axis orientations, and strong crustal anisotropy associated with mineral alignment during this process is resolved by Clement et al. (1994) via shear-wave splitting. On the other hand, local basins in East Greenland show W-E and NW-SE extension (Henriksen et al., 2009), the latter being perpendicular to the shallow a-axis orientations inferred here. This discrepancy may not be significant if orogenic deformation over longer length-scales dominates lithospheric fabrics relative to more localized rifting events.

Comparisons of SKS and SKKS measurements have shown that anisotropy in the lower mantle impacts measurements at station ALE (Dubé et al., 2020; Niu & Perez, 2004). Lower mantle anisotropy has also been imaged below Iceland and shown to impact differential SKS–SKKS measurements at Greenland stations (Wolf et al., 2019). There are two sets of measurements in our dataset for which we measure both SKS and SKKS phases for the same event-station pair (Table S2). One of these event pairs is from station NEEM for an event in 2019. For this measurement pair, an SKS–SKKS discrepancy is not resolved, given the uncertainties in the measurements. The other measurement pair is at station IVI and corresponds to an event in 2017. For this measurement pair, the splitting fast directions of the SKS and SKKS measurements are nearly perpendicular (offset by 94°), and the SKKS measurement has a splitting delay time that is larger by 0.9 s; this discrepancy may suggest a lowermost mantle contribution. However, a dataset larger than just these two SKS–SKKS pairs is needed to more rigorously discuss lower mantle contributions to splitting for our SKS measurements. Further work should also be conducted to constrain the extent to which anisotropy from crustal sources (e.g., Clement et al., 1994) may impact shear-wave splitting measurements.

## 5. Conclusions

Using 299 new splitting measurements from stations across Greenland, we have found a consistent pattern of splitting fast direction variation in back-azimuth which indicates the presence of multi-layer anisotropy. We used grid searches to solve for two-layer models of anisotropy that provide acceptable fits to the fast directions. Acceptable a-axis azimuths are 222–236° in the shallow layer and 114–130° in the deep layer.

A-axis azimuths in the shallow layer are consistent with lithospheric anisotropy due to Proterozoic and Archean orogenic events, as indicated by tectonic fabrics in western and northern Greenland. To explain anisotropy in the deeper model layer, we propose two scenarios. In one interpretation, anisotropy in the deeper layer represents asthenospheric shearing due to plate motion in a no-net-rotation reference frame; plunging asthenospheric a-axes may be due to flow being diverted by lithospheric basal topography and local, edge-driven convection. In another interpretation, anisotropy in the deeper layer represents dipping

layers of anisotropic lithosphere, underthrust during plate collisions. The clear and pronounced variations in the back-azimuthal pattern of fast directions in Greenland, combined with similar results in the Canadian high arctic (Dubé et al., 2020) is consistent with coherent lithospheric deformation from Proterozoic and Archean orogenesis on a broader scale than previously appreciated.

## Data Availability Statement

All seismic data used are freely available and can be downloaded from the IRIS DMC and GEOFON data archives at <https://ds.iris.edu/ds/nodes/dmc/> and <https://geofon.gfz-potsdam.de/waveform/archive/>, respectively. Network codes used include DK (the Danish Seismological Network, <http://www.fdsn.org/networks/detail/DK/>), GE (GEOFON, <https://doi.org/10.14470/TR560404>), XF (Operated by Columbia University, [https://doi.org/10.7914/SN/XF\\_2014](https://doi.org/10.7914/SN/XF_2014)), G (GEOSCOPE, <https://doi.org/10.18715/geoscope.g>), CN (Canadian National Seismograph Network, <https://doi.org/10.7914/SN/CN>), and II (the IRIS/IDA Global Seismographic Network, <https://doi.org/10.7914/SN/II>). Shear-wave splitting measurements were made using the Splitlab software package (Wüstefeld et al., 2008), accessible at <http://splitting.gm.univ-montp2.fr/>. Some figures were prepared with GMT software (Wessel & Smith, 1998). Information about stations used in this study and individual shear-wave splitting measurements used in this text are available as supplementary tables (Nathan et al., 2020).

## Acknowledgments

We thank James Hammond and an anonymous reviewer for their thoughtful comments, which improved the quality of the manuscript. We thank Isabella Gama, Hannah Krueger, Julia Krogh, and Ningli Zhao for assistance with making initial measurements. A.H. is supported by an NSF Graduate Research Fellowship under grant DGE-16-44760.

## References

- Abramson, E. H., Brown, J. M., Slutsky, L. J., & Zaug, J. (1997). The elastic constants of San Carlos olivine to 17 GPa. *Journal of Geophysical Research*, 102(B6), 12253–12263. <https://doi.org/10.1029/97jb00682>
- Abt, D. L., & Fischer, K. M. (2008). Resolving three-dimensional anisotropic structure with shear wave splitting tomography. *Geophysical Journal International*, 173(3), 859–886. <https://doi.org/10.1111/j.1365-246x.2008.03757.x>
- Abt, D. L., Fischer, K. M., Abers, G. A., Protti, M., González, V., & Strauch, W. (2010). Constraints on upper mantle anisotropy surrounding the Cocos slab from SK(K)S splitting. *Journal of Geophysical Research: Solid Earth*, 115(B6). <https://doi.org/10.1029/2009jb006710>
- Abt, D. L., Fischer, K. M., Abers, G. A., Strauch, W., Protti, J. M., & González, V. (2009). Shear wave anisotropy beneath Nicaragua and Costa Rica: Implications for flow in the mantle wedge. *Geochemistry, Geophysics, Geosystems*, 10(5). <https://doi.org/10.1029/2009gc002375>
- Amante, C., & Eakins, B. W. (2009). Etopo1 arc-minute global relief model: Procedures, data sources and analysis.
- Anderson, O. L., & Isaak, D. G. (1995). Elastic constants of mantle minerals at high temperature. In *Mineral physics and crystallography: A handbook of physical constants* (Vol. 2, pp. 64–97).
- Antonijevic, S. K., & Lees, J. M. (2018). Effects of the Iceland plume on Greenland's lithosphere: New insights from ambient noise tomography. *Polar Science*, 17, 75–82. <https://doi.org/10.1016/j.polar.2018.06.004>
- Aragon, J. C., Long, M. D., & Benoit, M. H. (2017). Lateral variations in SKS splitting across the magic array, central Appalachians. *Geochemistry, Geophysics, Geosystems*, 18(11), 4136–4155. <https://doi.org/10.1002/2017gc007169>
- Argus, D. F., Gordon, R. G., & DeMets, C. (2011). Geologically current motion of 56 plates relative to the no-net-rotation reference frame. *Geochemistry, Geophysics, Geosystems*, 12(11). <https://doi.org/10.1029/2011gc003751>
- Babuška, V., Plomerová, J., & Šílený, J. (1993). Models of seismic anisotropy in the deep continental lithosphere. *Physics of the Earth and Planetary Interiors*, 78(3–4), 167–191.
- Bak, J., Korstgård, J., & Sørensen, K. (1975). A major shear zone within the Nagssugtoqidian of West Greenland. *Tectonophysics*, 27(3), 191–209. [https://doi.org/10.1016/0040-1951\(75\)90016-5](https://doi.org/10.1016/0040-1951(75)90016-5)
- Bastow, I. D., Thompson, D. A., Wooley, J., Kendall, J.-M., Helffrich, G., Snyder, D. B., et al. (2011). Precambrian plate tectonics: Seismic evidence from northern Hudson Bay, Canada. *Geology*, 39(1), 91–94. <https://doi.org/10.1130/G31396.1>
- Bentley, C. R. (1972). Seismic-wave velocities in anisotropic ice: A comparison of measured and calculated values in and around the deep drill hole at Byrd Station, Antarctica. *Journal of Geophysical Research*, 77(23), 4406–4420. <https://doi.org/10.1029/jb077i023p04406>
- Braun, A., Kim, H. R., Csatho, B., & von Frese, R. R. (2007). Gravity-inferred crustal thickness of Greenland. *Earth and Planetary Science Letters*, 262(1–2), 138–158. <https://doi.org/10.1016/j.epsl.2007.07.050>
- Calixto, F. J., Robinson, D., Sandvol, E., Kay, S., Abt, D., Fischer, K., et al. (2014). Shear wave splitting and shear wave splitting tomography of the southern Puna plateau. *Geophysical Journal International*, 199(2), 688–699. <https://doi.org/10.1093/gji/gju296>
- Clement, W. P., Carbonell, R., & Smithson, S. B. (1994). Shear-wave splitting in the lower crust beneath the Archean crust of southwest Greenland. *Tectonophysics*, 232(1–4), 195–210. [https://doi.org/10.1016/0040-1951\(94\)90084-1](https://doi.org/10.1016/0040-1951(94)90084-1)
- Colli, L., Ghelichkhan, S., Bunge, H.-P., & Oeser, J. (2018). Retrodiction of Mid Paleogene mantle flow and dynamic topography in the Atlantic region from compressible high resolution adjoint mantle convection models: Sensitivity to deep mantle viscosity and tomographic input model. *Gondwana Research*, 53, 252–272. <https://doi.org/10.1016/j.gr.2017.04.027>
- Conrad, C. P., & Behn, M. D. (2010). Constraints on lithosphere net rotation and asthenospheric viscosity from global mantle flow models and seismic anisotropy. *Geochemistry, Geophysics, Geosystems*, 11(5). <https://doi.org/10.1029/2009GC002970>
- Dahl-Jensen, T., Larsen, T. B., Woelbern, I., Bach, T., Hanka, W., Kind, R., et al. (2003). Depth to Moho in Greenland: Receiver-function analysis suggests two Proterozoic blocks in Greenland. *Earth and Planetary Science Letters*, 205(3–4), 379–393. [https://doi.org/10.1016/s0012-821x\(02\)01080-4](https://doi.org/10.1016/s0012-821x(02)01080-4)
- Darbyshire, F. A., Bastow, I. D., Forte, A. M., Hobbs, T. E., Calvel, A., Gonzalez-Monteza, A., & Schow, B. (2015). Variability and origin of seismic anisotropy across eastern Canada: Evidence from shear wave splitting measurements. *Journal of Geophysical Research: Solid Earth*, 120(12), 8404–8421. <https://doi.org/10.1002/2015JB012228>

- Darbyshire, F. A., Dahl-Jensen, T., Larsen, T. B., Voss, P. H., & Joyal, G. (2018). Crust and uppermost-mantle structure of greenland and the northwest atlantic from Rayleigh wave group velocity tomography. *Geophysical Journal International*, 212(3), 1546–1569. <https://doi.org/10.1093/gji/ggx479>
- Dawes, P. R. (2009). The bedrock geology under the inland ice: The next major challenge for Greenland mapping. *Geological Survey of Denmark and Greenland Bulletin*, 17, 57–60.
- Debayle, E., & Ricard, Y. (2013). Seismic observations of large-scale deformation at the bottom of fast-moving plates. *Earth and Planetary Science Letters*, 376, 165–177. <https://doi.org/10.1016/j.epsl.2013.06.025>
- Dubé, J.-M., Darbyshire, F. A., Liddell, M. V., Stephenson, R., & Oakey, G. (2020). Seismic anisotropy of the Canadian high arctic: Evidence from shear-wave splitting. *Tectonophysics*, 789, 228524. <https://doi.org/10.1016/j.tecto.2020.228524>
- Ekström, G. (2011). A global model of love and Rayleigh surface wave dispersion and anisotropy, 25–250 s. *Geophysical Journal International*, 187(3), 1668–1686. <https://doi.org/10.1111/j.1365-246x.2011.05225.x>
- Fischer, K. M., Parmentier, E. M., Stine, A. R., & Wolf, E. R. (2000). Modeling anisotropy and plate-driven flow in the Tonga subduction zone back arc. *Journal of Geophysical Research*, 105(B7), 16181–16191. <https://doi.org/10.1029/1999jb900441>
- Forsyth, D., Morel-AL'Huissier, P., Asudeh, I., & Green, A. (1986). Alpha Ridge and iceland-products of the same plume? *Journal of Geodynamics*, 6(1–4), 197–214. [https://doi.org/10.1016/0264-3707\(86\)90039-6](https://doi.org/10.1016/0264-3707(86)90039-6)
- Fouch, M. J., Fischer, K. M., Parmentier, E. M., Wysession, M. E., & Clarke, T. J. (2000). Shear wave splitting, continental keels, and patterns of mantle flow. *Journal of Geophysical Research*, 105(B3), 6255–6275. <https://doi.org/10.1029/1999jb900372>
- Frisillo, A. L., & Barsch, G. R. (1972). Measurement of single-crystal elastic constants of bronzite as a function of pressure and temperature. *Journal of Geophysical Research*, 77(32), 6360–6384. <https://doi.org/10.1029/jb077i032p06360>
- Gripp, A. E., & Gordon, R. G. (1990). Current plate velocities relative to the hotspots incorporating the NUVEL-1 global plate motion model. *Geophysical Research Letters*, 17(8), 1109–1112. <https://doi.org/10.1029/gl017i008p01109>
- Grund, M., & Ritter, J. R. R. (2020). Shear-wave splitting beneath Fennoscandia—Evidence for dipping structures and laterally varying multilayer anisotropy. *Geophysical Journal International*, 223(3), 1525–1547. <https://doi.org/10.1093/gji/ggaa388>
- Harland, S. R., Kendall, J.-M., Stuart, G. W., Lloyd, G. E., Baird, A. F., Smith, A. M., et al. (2013). Deformation in Rutford Ice Stream, West Antarctica: measuring shear-wave anisotropy from icequakes. *Annals of Glaciology*, 54(64), 105–114. <https://doi.org/10.3189/2013aog64a033>
- Helffrich, G., Silver, P., & Given, H. (1994). Shear-wave splitting variation over short spatial scales on continents. *Geophysical Journal International*, 119(2), 561–573. <https://doi.org/10.1111/j.1365-246X.1994.tb00142.x>
- Henriksen, N., Higgins, A., Kalsbeek, F., & Pulvertaft, T. C. R. (2009). Greenland from Archean to quaternary. *Geological Survey of Denmark and Greenland Bulletin*, 18, 126. <https://doi.org/10.34194/geusb.v18.4993>
- Higgins, A. K., & Leslie, A. G. (2000). Restoring thrusting in the East Greenland Caledonides. *Geology*, 28(11), 1019–1022. [https://doi.org/10.1130/0091-7613\(2000\)028<1019:rtiteg>2.3.co;2](https://doi.org/10.1130/0091-7613(2000)028<1019:rtiteg>2.3.co;2)
- Hodges, K. V. (2016). Crustal decoupling in collisional orogenesis: Examples from the East Greenland Caledonides and Himalaya. *Annual Review of Earth and Planetary Sciences*, 44, 685–708. <https://doi.org/10.1146/annurev-earth-060115-012412>
- Holtzman, B. K., Kohlstedt, D. L., Zimmerman, M. E., Heidelbach, F., Hiraga, T., & Hustoft, J. (2003). Melt segregation and strain partitioning: Implications for seismic anisotropy and mantle flow. *Science*, 301(5637), 1227–1230. <https://doi.org/10.1126/science.1087132>
- Hung, S.-H., & Forsyth, D. W. (1998). Modeling anisotropic wave propagation in oceanic inhomogeneous structures using the parallel multi-domain pseudo-spectral method. *Geophysical Journal International*, 133, 726–740. <https://doi.org/10.1046/j.1365-246x.1998.00526.x>
- Karato, S.-i., Jung, H., Katayama, I., & Skemer, P. (2008). Geodynamic significance of seismic anisotropy of the upper mantle: New insights from laboratory studies. *Annual Review of Earth and Planetary Sciences*, 36, 59–95. <https://doi.org/10.1146/annurev.earth.36.031207.124120>
- Korstgård, J., Ryan, B., & Wardle, R. (1987). The boundary between Proterozoic and Archean crustal blocks in central West Greenland and northern Labrador. *Geological Society, London, Special Publications*, 27(1), 247–259. <https://doi.org/10.1144/gsl.sp.1987.027.01.21>
- Kumar, P., Kind, R., Hanka, W., Wylegalla, K., Reigber, C., & Yuan, X. (2005). The lithosphere–asthenosphere boundary in the North-West Atlantic region. *Earth and Planetary Science Letters*, 236(1–2), 249–257. <https://doi.org/10.1016/j.epsl.2005.05.029>
- Kumar, P., Kind, R., Priestley, K., & Dahl-Jensen, T. (2007). Crustal structure of Iceland and Greenland from receiver function studies. *Journal of Geophysical Research: Solid Earth*, 112(B3). <https://doi.org/10.1029/2005jb003991>
- Lawer, L. A., & Müller, R. D. (1994). Iceland hotspot track. *Geology*, 22(4), 311–314. [https://doi.org/10.1130/0091-7613\(1994\)022<0311:iht>2.3.co;2](https://doi.org/10.1130/0091-7613(1994)022<0311:iht>2.3.co;2)
- Lebedev, S., Schaeffer, A. J., Fullea, J., & Pease, V. (2018). Seismic tomography of the arctic region: Inferences for the thermal structure and evolution of the lithosphere. *Geological Society, London, Special Publications*, 460(1), 419–440. <https://doi.org/10.1144/sp460.10>
- Levin, V., Menke, W., & Park, J. (1999). Shear wave splitting in the Appalachians and the Urals: A case for multilayered anisotropy. *Journal of Geophysical Research*, 104(B8), 17975–17993. <https://doi.org/10.1029/1999jb900168>
- Levshin, A., Ritzwoller, M., Barmin, M., Villasenor, A., & Padgett, C. (2001). New constraints on the arctic crust and uppermost mantle: Surface wave group velocities, Pn, and Sn. *Physics of the Earth and Planetary Interiors*, 123(2–4), 185–204. [https://doi.org/10.1016/s0031-9201\(00\)00209-0](https://doi.org/10.1016/s0031-9201(00)00209-0)
- Levshin, A., Shen, W., Barmin, M., & Ritzwoller, M. (2017). Surface wave studies of the Greenland upper lithosphere using ambient seismic noise. *Pure and Applied Geophysics*, 174.
- Liddell, M. V., Bastow, I., Darbyshire, F., Gilligan, A., & Pugh, S. (2017). The formation of Laurentia: Evidence from shear wave splitting. *Earth and Planetary Science Letters*, 479, 170–178. <https://doi.org/10.1016/j.epsl.2017.09.030>
- Long, M. D., & Becker, T. W. (2010). Mantle dynamics and seismic anisotropy. *Earth and Planetary Science Letters*, 297(3–4), 341–354. <https://doi.org/10.1016/j.epsl.2010.06.036>
- Long, M. D., De Hoop, M. V., & Van Der Hilst, R. D. (2008). Wave-equation shear wave splitting tomography. *Geophysical Journal International*, 172(1), 311–330. <https://doi.org/10.1111/j.1365-246x.2007.03632.x>
- Mainprice, D., & Silver, P. G. (1993). Interpretation of SKS-waves using samples from the subcontinental lithosphere. *Physics of the Earth and Planetary Interiors*, 78(3–4), 257–280. [https://doi.org/10.1016/0031-9201\(93\)90160-b](https://doi.org/10.1016/0031-9201(93)90160-b)
- Marquart, G., Schmeling, H., & Čadek, O. (2007). Dynamic models for mantle flow and seismic anisotropy in the North Atlantic region and comparison with observations. *Geochemistry, Geophysics, Geosystems*, 8(2). <https://doi.org/10.1029/2006GC001359>
- Martos, Y. M., Jordan, T. A., Catalán, M., Jordan, T. M., Bamber, J. L., & Vaughan, D. G. (2018). Geothermal heat flux reveals the Iceland hotspot track underneath Greenland. *Geophysical Research Letters*, 45(16), 8214–8222. <https://doi.org/10.1029/2018GL078289>
- Mihalffy, P., Steinberger, B., & Schmeling, H. (2008). The effect of the large-scale mantle flow field on the Iceland hotspot track. *Tectonophysics*, 447(1–4), 5–18. <https://doi.org/10.1016/j.tecto.2006.12.012>

- Miller, M. S., & Becker, T. W. (2012). Mantle flow deflected by interactions between subducted slabs and Cratonic keels. *Nature Geoscience*, 5(10), 726–730. <https://doi.org/10.1038/ngeo1553>
- Mondal, P., & Long, M. D. (2020). Strong seismic anisotropy in the deep upper mantle beneath the Cascadia backarc: Constraints from probabilistic finite-frequency SKS splitting intensity tomography. *Earth and Planetary Science Letters*, 539, 116172. <https://doi.org/10.1016/j.epsl.2020.116172>
- Mordret, A. (2018). Uncovering the Iceland hot spot track beneath Greenland. *Journal of Geophysical Research: Solid Earth*, 123(6), 4922–4941. <https://doi.org/10.1029/2017jb015104>
- Nathan, E., Hariharan, A., Florez, D., & Fischer, K. (2020). *Supplementary data tables for multilayer seismic anisotropy beneath Greenland*. Brown University Open Data Collection. Brown Digital Repository. Brown University Library. <https://doi.org/10.7910/DVN/XB4SCT>
- Niu, F., & Perez, A. M. (2004). Seismic anisotropy in the lower mantle: A comparison of waveform splitting of SKS and SKKS. *Geophysical Research Letters*, 31(24). <https://doi.org/10.1029/2004gl021196>
- Pourpoint, M., Anandakrishnan, S., & Ammon, C. J. (2018). High-resolution Rayleigh wave group velocity variation beneath Greenland. *Journal of Geophysical Research: Solid Earth*, 123(2), 1516–1539. <https://doi.org/10.1002/2017jb015072>
- Sanborn-Barrie, M., Thrane, K., Wodicka, N., & Rayner, N. (2017). The Laurentia – West Greenland connection at 1.9 Ga: New insights from the Rinkian fold belt. *Gondwana Research*, 51, 289–309. <https://doi.org/10.1016/j.gr.2017.07.002>
- Savage, M. K., & Silver, P. G. (1993). Mantle deformation and tectonics: Constraints from seismic anisotropy in the western United States. *Physics of the Earth and Planetary Interiors*, 78(3–4), 207–227. [https://doi.org/10.1016/0031-9201\(93\)90156-4](https://doi.org/10.1016/0031-9201(93)90156-4)
- Schaeffer, A. J., Lebedev, S., & Becker, T. W. (2016). Azimuthal seismic anisotropy in the Earth's upper mantle and the thickness of tectonic plates. *Geophysical Journal International*, 207(2), 901–933. <https://doi.org/10.1093/gji/ggw309>
- Schiffer, C., Balling, N., Jacobsen, B. H., Stephenson, R. A., & Nielsen, S. B. (2014). Seismological evidence for a fossil subduction zone in the East Greenland Caledonides. *Geology*, 42(4), 311–314. <https://doi.org/10.1130/g35244.1>
- Servali, A., Long, M. D., Park, J., Benoit, M. H., & Aragon, J. C. (2020). Love-to-Rayleigh scattering across the Eastern North American passive margin. *Tectonophysics*, 776, 228321.
- Seton, M., Müller, R. D., Zahirovic, S., Gaina, C., Torsvik, T., Shephard, G., et al. (2012). Global continental and ocean basin reconstructions since 200 Ma. *Earth-Science Reviews*, 113(3–4), 212–270. <https://doi.org/10.1016/j.earscirev.2012.03.002>
- Silver, P. G. (1996). Seismic anisotropy beneath the continents: Probing the depths of geology. *Annual Review of Earth and Planetary Sciences*, 24(1), 385–432.
- Silver, P. G., & Chan, W. W. (1991). Shear wave splitting and subcontinental mantle deformation. *Journal of Geophysical Research: Solid Earth*, 96(B10), 16429–16454.
- Silver, P. G., & Savage, M. K. (1994). The interpretation of shear-wave splitting parameters in the presence of two anisotropic layers. *Geophysical Journal International*, 119(3), 949–963.
- Smith, E. C., Baird, A. F., Kendall, J. M., Martín, C., White, R. S., Brisbourne, A. M., & Smith, A. M. (2017). Ice fabric in an Antarctic Ice Stream interpreted from seismic anisotropy. *Geophysical Research Letters*, 44(8), 3710–3718.
- Snedecor, G. W., & Cochran, W. G. (1991). *Statistical methods*. John Wiley & Sons.
- Snyder, D. B., Berman, R. G., Kendall, J. M., & Sanborn-Barrie, M. (2013). Seismic anisotropy and mantle structure of the Rae craton, central Canada, from joint interpretation of SKS splitting and receiver functions. *Precambrian Research*, 232, 189–208. <https://doi.org/10.1016/j.precamres.2012.03.003>
- Steffen, R., Audet, P., & Lund, B. (2018). Weakened lithosphere beneath Greenland inferred from effective elastic thickness: A hot spot effect? *Geophysical Research Letters*, 45(10), 4733–4742.
- Steinberger, B., & Becker, T. W. (2018). A comparison of lithospheric thickness models. *Tectonophysics*, 746, 325–338.
- Steinberger, B., Bredow, E., Lebedev, S., Schaeffer, A., & Torsvik, T. H. (2019). Widespread volcanism in the Greenland–North Atlantic region explained by the Iceland plume. *Nature Geoscience*, 12(1), 61–68.
- St-Onge, M. R., Van Gool, J. A., Garde, A. A., & Scott, D. J. (2009). Correlation of Archean and Palaeoproterozoic units between north-eastern Canada and western Greenland: Constraining the pre-collisional upper plate accretionary history of the Trans-Hudson orogen. *Geological Society, London, Special Publications*, 318(1), 193–235.
- Thorsteinsson, T. (2000). Anisotropy of ice Ih: Development of fabric and effects of anisotropy on deformation (Doctoral dissertation).
- Thorsteinsson, T., Kipfstuhl, J., & Miller, H. (1997). Textures and fabrics in the grip ice core. *Journal of Geophysical Research: Oceans*, 102(C12), 26583–26599.
- Till, C. B., Elkins-Tanton, L. T., & Fischer, K. M. (2010). A mechanism for low-extent melts at the lithosphere–asthenosphere boundary. *Geochemistry, Geophysics, Geosystems*, 11(10).
- Toyokuni, G., Matsuno, T., & Zhao, D. (2020). P-wave tomography beneath Greenland and surrounding regions—I. Crust and upper mantle. *Journal of Geophysical Research: Solid Earth*, 125(12), e2020JB019837. <https://doi.org/10.1029/2020JB019837>
- Ucikis, N., Gudmundsson, Ó., Hanka, W., Dahl-Jensen, T., Mosegaard, K., & Priestley, K. (2008). Variations of shear-wave splitting in Greenland: Mantle anisotropy and possible impact of the Iceland plume. *Tectonophysics*, 462(1–4), 137–148.
- Ucikis, N., Gudmundsson, Ó., Priestley, K., & Larsen, T. B. (2005). Seismic anisotropy beneath East Greenland revealed by shear wave splitting. *Geophysical Research Letters*, 32(8).
- van Gool, J. A., Connelly, J. N., Marker, M., & Mengel, F. C. (2002). The Nagssugtoqidian orogen of West Greenland: Tectonic evolution and regional correlations from a West Greenland perspective. *Canadian Journal of Earth Sciences*, 39(5), 665–686.
- Vinnik, L., Makeyeva, L., Milev, A., & Usenko, A. Y. (1992). Global patterns of azimuthal anisotropy and deformations in the continental mantle. *Geophysical Journal International*, 111(3), 433–447.
- Vinnik, L. P., Farra, V., & Romanowicz, B. (1989). Azimuthal anisotropy in the earth from observations of SKS at GEOSCOPE and NARS broadband stations. *Bulletin of the Seismological Society of America*, 79(5), 1542–1558.
- Von Gosen, W., Piepjohn, K. (1999). Evolution of the Kap Cannon thrust zone (north Greenland). *Tectonics*, 18(6), 1004–1026.
- Wüstefeld, A., Bokelmann, G., Zaroli, C., & Barruol, G. (2008). SplitLab: A shear-wave splitting environment in Matlab. *Computers & Geosciences*, 34(5), 515–528.
- Walsh, E., Arnold, R., & Savage, M. (2013). Silver and Chan revisited. *Journal of Geophysical Research: Solid Earth*, 118(10), 5500–5515.
- Wessel, P., & Smith, W. H. (1998). New, improved version of generic mapping tools released. *Eos, Transactions American Geophysical Union*, 79(47), 579579.
- Wolf, J., Creasy, N., Pisconti, A., Long, M. D., & Thomas, C. (2019). An investigation of seismic anisotropy in the lowermost mantle beneath Iceland. *Geophysical Journal International*, 219(Supplement\_1), S152–S166.

- Wookey, J. (2012). Direct probabilistic inversion of shear wave data for seismic anisotropy. *Geophysical Journal International*, 189, 1025–1037. <https://doi.org/10.1111/j.1365-246X.2012.05405.x>
- Yuan, H., & Levin, V. (2014). Stratified seismic anisotropy and the lithosphere-asthenosphere boundary beneath eastern North America. *Journal of Geophysical Research: Solid Earth*, 119(4), 3096–3114.